Combustion and Flame 157 (2010) 2063–2077

Contents lists available at ScienceDirect

Combustion and Flame

journal homepage: www.elsevier.com/locate/combustflame

Simulations of flame acceleration and deflagration-to-detonation transitions in methane–air systems

D.A. Kessler *, V.N. Gamezo, E.S. Oran

Laboratory for Computational Physics and Fluid Dynamics, Naval Research Laboratory, Washington, DC, United States

ARTICLE INFO

Article history:
Received 2 February 2010
Received in revised form 17 March 2010
Accepted 16 April 2010
Available online 13 May 2010

Keywords:
Deflagration-to-detonation transition
Methane–air explosions
Flame acceleration
Obstructed channels

ABSTRACT

Flame acceleration and deflagration-to-detonation transitions (DDT) in large obstructed channels filled with a stoichiometric methane–air mixture are simulated using a single-step reaction mechanism. The reaction parameters are calibrated using known velocities and length scales of laminar flames and detonations. Calculations of the flame dynamics and DDT in channels with obstacles are compared to previously reported experimental data. The results obtained using the simple reaction model qualitatively, and in many cases, quantitatively match the experiments and are found to be largely insensitive to small variations in model parameters.

Published by Elsevier Inc. on behalf of The Combustion Institute.

1. Introduction

The atmospheres of confined regions in underground facilities, such as sealed-off tunnels and chambers in mining operations, can develop into potentially explosive mixtures of natural gas and air. Explosions in these regions are a significant concern because of the extent to which they may harm personnel, equipment, and the production process. This paper describes the first steps we have taken in developing a multidimensional numerical model to study explosions in large-scale systems containing mixtures of natural gas and air. This final model must have the ability to compute the different stages of the evolution of a chemically reactive flow: ignition by a small spark, rapid flame acceleration, development of shocks, shock–flame interactions, and detonation initiation in complex geometries for natural gas mixtures with spatially and temporally-varying stoichiometries. Here we describe the first few steps toward achieving this objective.

Numerical models that can describe the behavior of shocks and detonations vary widely in their complexity, but for many practical situations, an extensive description of the details of the chemical pathways is unnecessary. Instead, it is more important to have an accurate model of the fluid dynamics coupled to a model for the chemical-energy release that puts the released energy in the "right" place in the flow at the "right" time. For example, ignition behind a shock forming a detonation wave can be quantitatively predicted if an acceptable representation of the chemical induction time is known as a function of the state variables, temperature, and pressure. This observation led to the development of single-step reaction models, such as the induction-parameter model [1], and, later, to reduced two- and three-step chain-branching reaction models [2]. While these models have been quite successful for computing steady-state and certain transient properties of detonations, they generally cannot be used for calculating properties of flames for which diffusion and thermal conduction are important. They are not appropriate for combustion wave transitions, such as the transition from a laminar to turbulent flame or a turbulent flame to a detonation.

Thus, numerical simulations involving flames require some treatment of diffusion processes in addition to chemical reaction and energy release. This can be done with high accuracy using detailed chemical reaction mechanisms, if they are known, although the computational price can be so high that it severely limits the extent of a calculation. For this reason, it becomes much too expensive to use a detailed reaction mechanism to compute flames in large physical systems. An enormous amount of work has been done to find reduced chemical models for hydrogen and hydrocarbons that work well when coupled to fluid codes. Usually, this amounts to finding the minimal set of reactions that are critical for describing the flame structure for a particular fuel mixture [3–6]. A different approach is to assume that the complex set of reactions can be modeled by a generic set of global reactions [7–9]. For example, the widely used model developed by Westbrook and Dryer [7] is based on a single-step Arrhenius reaction,

$$\Omega = A\exp(-E_a/RT)[\text{Fuel}]^a[\text{Oxidizer}]^b \quad (1)$$

where $[m]$ represents the concentration of species m. The model parameters, A, E_a, a, and b, are calibrated for a particular fuel based on measured lean and rich explosion limits and the laminar flame

* Corresponding author.

0010-2180/$ - see front matter Published by Elsevier Inc. on behalf of The Combustion Institute.
doi:10.1016/j.combustflame.2010.04.011

speed. While this expression sometimes gives results that agree reasonably well with experiments for laminar flames, it does not work for calculating properties of detonations. Some progress, however, has been made toward developing a four-step mechanism for hydrogen–oxygen mixtures that is valid for both flames and detonations [10].

Here we address the problem of developing a minimal model that captures the essential features of a flame, a detonation, and the deflagration-to-detonation transition (DDT) in methane–air mixtures. In previous work, we described similar single-step models for low-pressure acetylene, low-pressure ethylene, and atmospheric-pressure hydrogen–air mixtures [11–17]. Using these models in calculations taught us a great deal about basic physical processes governing turbulent flame acceleration and DDT, as summarized in [15], and in high-speed turbulence [18]. Now we are interested in extending this approach to methane and natural gas.

The work in this paper is focused on developing and testing a chemical-diffusion model, which, when coupled to an appropriate model for the fluid dynamics, will be accurate enough to simulate the transition of a low-speed flame to a detonation wave in a large, confined area containing a methane–air mixture. To do this, we have taken the same approach that was used previously for acetylene, ethylene, and hydrogen: we fit parameters so that they reproduce experimental and theoretical length and time scales of laminar flames and detonations. In the remainder of this paper, we describe and analyze the calibration process and then compare calculations of DDT in an obstructed channel to data from previously reported experiments [19,20].

2. Model

The reactants are assumed to be fully premixed and behave as an ideal gas, so that the flow is governed by the compressible reactive Navier-Stokes equations,

$$\frac{\partial \rho}{\partial t}+\frac{\partial \rho u}{\partial x}+\frac{\partial \rho v}{\partial y}=0, \tag{2}$$

$$\frac{\partial \rho u}{\partial t}+\frac{\partial \rho u u}{\partial x}+\frac{\partial \rho u v}{\partial y}=-\frac{\partial P}{\partial x}+\frac{\partial}{\partial x}\left[\rho \nu\left(\frac{4}{3}\frac{\partial u}{\partial x}-\frac{2}{3}\frac{\partial v}{\partial y}\right)\right]+\frac{\partial}{\partial y}\left[\rho \nu\left(\frac{\partial u}{\partial y}+\frac{\partial v}{\partial x}\right)\right], \tag{3}$$

$$\frac{\partial \rho v}{\partial t}+\frac{\partial \rho u v}{\partial x}+\frac{\partial \rho v v}{\partial y}=-\frac{\partial P}{\partial y}+\frac{\partial}{\partial x}\left[\rho \nu\left(\frac{\partial u}{\partial y}+\frac{\partial v}{\partial x}\right)\right]+\frac{\partial}{\partial y}\left[\rho \nu\left(\frac{4}{3}\frac{\partial v}{\partial y}-\frac{2}{3}\frac{\partial u}{\partial x}\right)\right], \tag{4}$$

$$\begin{aligned}\frac{\partial \rho e}{\partial t}+\frac{\partial}{\partial x}[(\rho e+P)u]+\frac{\partial}{\partial y}[(\rho e+P)v] &= \frac{\partial}{\partial x}\left[K\frac{\partial T}{\partial x}\right]+\frac{\partial}{\partial y}\left[K\frac{\partial T}{\partial y}\right]\\ &+\frac{\partial}{\partial x}\left[u\rho\nu\left(\frac{4}{3}\frac{\partial u}{\partial x}-\frac{2}{3}\frac{\partial v}{\partial y}\right)+v\rho\nu\left(\frac{\partial u}{\partial y}+\frac{\partial v}{\partial x}\right)\right]\\ &+\frac{\partial}{\partial y}\left[u\rho\nu\left(\frac{\partial u}{\partial y}+\frac{\partial v}{\partial x}\right)+v\rho\nu\left(\frac{4}{3}\frac{\partial v}{\partial y}-\frac{2}{3}\frac{\partial u}{\partial x}\right)\right]+q\Omega,\end{aligned} \tag{5}$$

$$\frac{\partial \rho Y}{\partial t}+\frac{\partial u\rho Y}{\partial x}+\frac{\partial v\rho Y}{\partial y}=\frac{\partial}{\partial x}\left[\rho D\frac{\partial Y}{\partial x}\right]+\frac{\partial}{\partial y}\left[\rho D\frac{\partial Y}{\partial y}\right]-\Omega, \tag{6}$$

$$P=\rho RT, \tag{7}$$

$$\rho e=\frac{P}{\gamma-1}+\frac{1}{2}\rho(u^2+v^2), \tag{8}$$

where ρ, T, u, v, P, e, q, and Y are the density, temperature, streamwise velocity, transverse velocity, pressure, specific energy, heat release, and fuel mass fraction of the gas mixture, respectively. The transport coefficients, viscosity ν, mass diffusivity D, and thermal diffusivity $\kappa = K/\rho\, c_p$, where K is the thermal conductivity, vary with temperature according to

$$\begin{aligned}\nu &= \nu_o\frac{T^n}{\rho},\\ D &= D_o\frac{T^n}{\rho},\\ \kappa &= \kappa_o\frac{T^n}{\rho}.\end{aligned} \tag{9}$$

The parameters ν_o, D_o, and κ_o are assumed to be constant, and n is a constant chosen to be 0.7. In this model, the ratio of specific heats γ does not vary with temperature.

We use a one-step Arrhenius chemistry model such that the reaction rate Ω is given by

$$\Omega = A\rho Y\exp(-E_a/RT), \tag{10}$$

where A is the pre-exponential factor, R is the gas constant, and E_a is the activation energy for the reaction. This equation is similar to Eq. (1) with $a = 1$ and $b = 0$. This type of reaction model has been used in past work for acetylene, ethylene, and hydrogen to solve a variety of combustion and detonation problems involving shock–flame interactions and to compute the properties of the cellular structure of detonations [11–14,17,16,21,15,22–24]. In this model, there is no explicit description of radiative diffusion; however, some radiation effects could be implicitly contained in the adjustable parameters. Energy losses through boundaries are neglected.

3. Model parameter calibration

The one-step Arrhenius kinetics used in this model cannot exactly reproduce all properties of laminar flames and detonations in methane–air mixtures. The model can, however, give a reasonable approximation of the key length and time scales involved at different stages of DDT [15]. During the first stage, an initially laminar flame is accelerated to a high-speed, turbulent deflagration wave. The second stage involves the formation of localized regions of elevated temperatures (hot spots) and subsequent detonation initiation by the Zeldovich gradient mechanism [25]. If the newly formed detonation survives, it spreads to the rest of the unburned material during the third stage.

Flame acceleration (in the laboratory frame) occurs primarily due to advection by the induced gas flow, which can be orders of magnitude larger than the laminar and turbulent flame speeds [17,16]. The gas flow is driven by thermal expansion of the combustion products and increases with the amount of heat released by the flame front, which is a function of the surface area of the flame. The flame-surface area increases due to stretching by the flow and wrinkling caused by turbulent motions and fluid-dynamic instabilities. When the flow speed approaches the speed of sound, shocks form, and shock–flame interactions become an important mechanism for the flame wrinkling and turbulence generation.

Based on this progression of physical processes, the properties of the fuel–air mixture that are important during this period of flame acceleration are the laminar flame speed, the adiabatic flame temperature, the viscosity, and the speed of sound. We restrict the discussion to mixtures of ideal gases, so that the sound speed is given by the expression $c=\sqrt{\gamma RT}$, and the specific heat capacity at constant pressure is related to the gas constant by $c_p = \gamma R/(\gamma-1)$. The temperature rise in an adiabatic system due to chemical-energy release is $T_b - T_o = q/c_p = q(\gamma-1)/\gamma\ R$. Thus, the adiabatic flame temperature T_b depends on the initial system temperature

T_o, the heat release q, and the ratio of specific heats γ. The laminar flame speed S_l depends on A, E_a, q, and κ.

Hot spots, which can evolve to generate flames, shocks, and detonations, may arise in unreacted material from many types of interactions in a turbulent, shock-laden reactive flow. In previous simulations, we observed them, for example, in shock reflections, vortices behind Mach stems, and multiply-shocked regions of unreacted material. In these hot regions, a spatial temperature gradient exists, and the temperature can be high enough to ignite the reactants. In the presence of the temperature gradient, ignition occurs consecutively in multiple layers of material heated to different temperatures, thus forming a reaction wave [25]. This wave can generate a strong shock and eventually a detonation. The survival of the newly formed detonation wave then depends on local thermal and chemical conditions and geometrical constraints [15].

These stages of DDT are controlled by induction delays behind strong shocks and properties of detonation waves. Since induction delays correlate with detonation cell sizes, a model calibrated on detonation properties should approximately describe key phenomena responsible for these final stages of DDT. The detonation properties used for the calibration are the theoretical Chapman–Jouget (CJ) detonation velocity D_{CJ} and the detonation cell size λ. The velocity D_{CJ} depends on the heat release q and γ. If the sound speed is correct, D_{CJ} gives an indication of the correct value of q, as T_b does for a deflagration. Then λ is controlled by A and E_a.

The model calibration is started by performing a series of one-dimensional calculations of flame and detonation structures for a range of input parameters. Then we choose a set of parameters that most closely reproduces *both* the laminar flame properties and the detonation properties. After this, two-dimensional simulations are used to compute detonation cell sizes using the model parameters arrived upon in the previous step. Finally, full simulations using the model parameters are used to compute flame acceleration and DDT, and these results are compared to experiments.

3.1. Laminar flames

First, the values of ν_0 and κ_0 are calculated directly from known viscosity and thermal conductivity of air at $T = 298$ K and $P = 1$ atm. For simplicity, we assume the Lewis number of the mixture is equal to unity, implying $D_0 = \kappa_0$, which is an acceptable approximation for premixed methane and air. We then compute properties of a one-dimensional laminar flame by solving an ordinary differential equation describing thermal conduction and energy release inside a steady-state reaction wave,

$$\frac{dF_t}{dx} = \rho\left(UC_p\frac{dT}{dx} - q\Omega\right), \tag{11}$$

$$F_t = K\frac{dT}{dx}, \tag{12}$$

where $U = S_l\rho_0/\rho$ is the flow velocity in the frame moving with the flame. According to Eq. (9), the thermal conductivity K is a function of temperature, $K = k_0T^{0.7}C_p$, where $C_p = R\gamma/(\gamma - 1)$. Details of the solution method are given in Appendix A and [21]. We search for a set of parameters, A, q, E_a, and γ, for which the computed value of S_l matches experimental data [26,27], and that of T_b matches values calculated using a complex reaction mechanism for methane–air combustion [28]. The laminar flame thickness, x_f, is based on the temperature gradient, i.e., $x_f = (T_b - T_0)/\max|\partial T/\partial x|$.

3.2. One-dimensional detonations

We use a Zeldovich–von Neumann–Doering (ZND) model to compute the half-reaction thickness of one-dimensional detonations using the same reaction model described in §2 for a set of parameters A, E_a, γ, and q. The reaction zone of a one-dimensional detonation is described by

$$\frac{d\rho}{dt} = \frac{q\Omega\rho(\gamma - 1)}{U^2 - c^2}, \tag{13}$$

$$\frac{de}{dt} = \frac{P}{\rho^2}\frac{d\rho}{dt} + q\Omega, \tag{14}$$

$$\frac{dx}{dt} = U, \tag{15}$$

where t is time, x the distance from the shock, $U = D_{CJ}\rho_0/\rho$ the flow velocity in the shock frame, $c = \sqrt{\gamma P/\rho}$ the sound speed, and

$$D_{CJ} = c_0\left(\sqrt{1 + \frac{q}{P_0}\frac{\rho_0(\gamma^2 - 1)}{2\gamma}} + \sqrt{\frac{q}{P_0}\frac{\rho_0(\gamma^2 - 1)}{2\gamma}}\right) \tag{16}$$

is the Chapman–Jouget detonation velocity. The solution procedure for this set of equations is described in Appendix B and [21].

Solutions of Eqs. (13)–(16) give the reaction-zone profile, from which we find the half-reaction thickness of the one-dimensional detonation wave, x_d. This quantity correlates with the detonation cell size λ [29], which is often measured in detonation experiments. Even though detonation cells do not develop until after DDT occurs, λ is generally used instead of x_d in empirical correlations related to the detonation initiation and DDT [30–41]. For example, experimental evidence suggests that the ratio of the system size to λ must be greater than one for a sustained detonation to occur [30]. As we did for the laminar flames, we use measured values of λ [19] (and, equivalently, x_d) and values of D_{CJ} calculated using a thermodynamic equilibrium code [42] to find a set of consistent model parameters.

3.3. Composite model

The choice of parameters γ and q determines T_b for laminar flames and D_{CJ} for one-dimensional detonations. Curves representing values of q that give $T_b = 2210$ K and $D_{CJ} = 1820$ m/s as a function of γ are shown in Fig. 1a. We choose the values of q and γ at the intersection of these two curves to use in our model. The remaining parameters, E_a and A, determine S_l and x_d for fixed κ_0, γ and q. Fig. 1b shows the values of A for which $S_l = 38.02$ cm/s and $x_d = 0.229$ cm as a function of E_a. Again, we choose A and E_a at the point of intersection of these curves. The results of this one-dimensional calibration process are given in Table 1 for a stoichiometric (9.5%) methane–air mixture. The computed input parameters and the resulting output for S_l, T_b, D_{CJ}, and λ are shown along with values of these parameters from the literature. We note that the determination of λ for high-activation-energy mixtures is not precise because the detonation cells are highly irregular. Hence, ranges for λ and x_d are given. The value of $x_d = 0.229$ cm used in the calibration process was chosen as a representative value within the range shown in Table 1. In practice, a range of E_a and A would give satisfactory values of λ.

3.4. Two-dimensional detonation cells

High-resolution, two-dimensional simulations of a detonation propagating in a planar channel [43] were performed using the model parameters chosen in the previous section. The computational cell size at the detonation front was chosen so that 234 cells spanned x_d. This level of grid refinement was necessary to properly resolve the transverse wave structures that generate the characteristic cellular pattern as an unstable detonation propagates. The detonation cells that formed were highly irregular, ranging in size from 10 to 20 cm. Fig. 2 shows a sequence of density contours over a distance equivalent to several detonation cell widths. In this example, the maximum distance between two adjacent triple

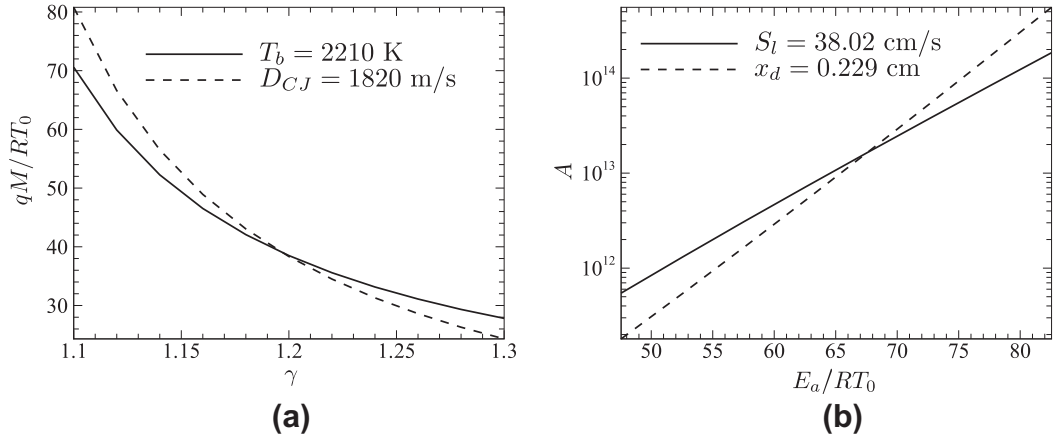

Fig. 1. Parametric curves for which (a) T_b = 2210 K, D_{CJ} = 1820 m/s and (b) S_l = 38.02 cm/s, x_d = 0.229 cm. The points of intersection in the two figures give the values of qM/RT_0, γ, E_a/RT_0, and A used in conjunction with the reaction model (Eq. (10)).

Table 1
Input model parameters and computed properties of reaction waves for stoichiometric methane–air mixture.

Input		
P_0	1 atm	
T_0	298 K	
M	27 g/mol	
γ	1.197	
A	1.64×10^{13} cm^3/g s	
E_a	$67.55RT_0$	
q	$39.0RT_0/M$	
ν_0	3.6×10^{-6} g/s cm K$^{0.7}$	
$\kappa_0 = D_0$	6.25×10^{-6} g/s cm K$^{0.7}$	
Output		
	Calculated values	Target values
S_l	38.02 cm/s	34–45 cm/s [26,27]
T_b	2210 K	2200–2230 K [28]
x_f	0.0439 cm	
D_{CJ}	1820 m/s	~1815 m/s [42]
x_d (λ)	0.229 cm (16–23 cm)*	0.13–0.62 cm (13–31 cm) [19]

* Based on estimated ratio of $50 \lesssim \lambda/x_d \lesssim 100$ [29].

points is approximately 16 cm, but this distance varies as the detonation propagates and new triple points form, giving rise to the range of cell sizes discussed above. The sizes of the computed cells are consistent with the range 13–31 cm observed in experiments [19]. The computed ratio of λ/x_d for this model is in the range of 43–87, which is consistent with previous calculations [29]. Thus, the chemistry model with coefficients calibrated using one-dimensional models produces two-dimensional detonations with length and time scales consistent with experimental observations.

4. Two-dimensional channels with obstacles

We next use this calibrated model to calculate multidimensional, turbulent, accelerating flames and subsequent DDT. Obstructed channels promote faster flame acceleration than smooth channels and, hence, provide a convenient testbed for studying DDT. In addition, this configuration has been used for several experimental studies, and so there is some data that can be used for comparisons.

The model planar 2D channel used in the calculations is shown in Fig. 3. The channel is closed at the left end ($x = 0$) and can either be open to the atmosphere or closed at the opposite end ($x = L$). At the bottom plane ($y = 0$) and the $x = 0$ boundary, we assume a nonslip, adiabatic wall, i.e., $u = v = 0$ and $\partial T/\partial n = \partial Y/\partial n = 0$, where n denotes the direction normal to the surface. The same nonslip

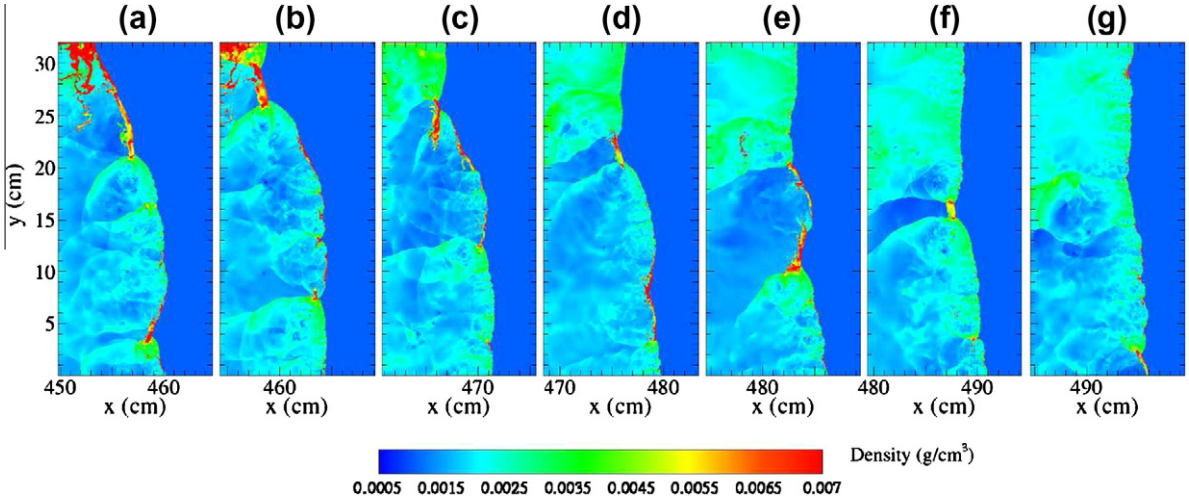

Fig. 2. Selected density maps near the reaction front of a detonation propagating through a 32 cm wide by 1024 cm long channel filled with a stoichiometric mixture of methane and air calculated using the reaction model (Eq. (10)) and the calibrated parameters listed in Table 1 at times t = (a) 2.480 ms, (b) 2.505 ms, (c) 2.542 ms, (d) 2.586 ms, (e) 2.620 ms, (f) 2.648 ms, and (g) 2.677 ms.

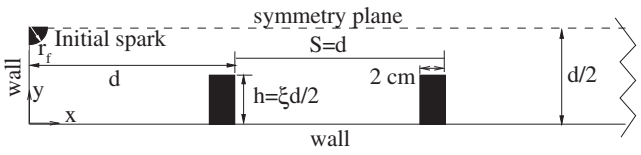

Fig. 3. Computational setup. Obstacles are evenly spaced along the entire length of the channel. Walls and obstacle surfaces are adiabatic no-slip reflecting boundaries. Initial flame radius is 0.25 cm.

boundary conditions are imposed along the face of every obstacle and at the right boundary $x = L$ for a closed channel. For an open channel, a zero-gradient outflow boundary condition was imposed at $x = L$. We assume the channel is symmetric and simulate only the lower half, so symmetry conditions $\partial u/\partial y = \partial Y/\partial\ y = \partial T/\partial y = \partial P/\partial y = v = 0$ are applied at the channel center line, $y = d/2$. The obstacles are taken to be 2 cm thick, and their heights are set based on the desired blockage ratio, $\xi = 2h/d$. Obstacle spacings S are set equal to d.

We consider three different configurations chosen to be similar to experimental systems [19,20] and summarized in Table 2. In the first configuration, $L = 216.2$ cm and $d = 7.6$ cm, which models the 7.6×7.6 cm square channel used in [20]. In those experiments, both ends of the channel were closed, and the initial pressure in the unburned gas mixture was 47 kPa. The second is a slightly larger channel with $d = 17.4$ cm and $L = 1187.8$ cm, which is similar to the circular cross-section tube (diameter 17.4 cm) used in [19]. Here, the right end of the channel is open to the atmosphere, and the initial gas pressure is atmospheric, as in the experiments. The third configuration ($d = 52$ cm, $L = 2130$ cm) is similar to the 52 cm diameter tube used in [19], where the channel is also open to the atmosphere at $x = L$. For each test case, the channel is uniformly filled with a stoichiometric methane–air mixture.

To ignite the mixture, we place a quarter-circular region of hot, burned material at the left wall on the centerline and add a small amount of extra energy to the burned region. The additional energy per unit mass is on the order of the chemical-energy release q, which could model ignition by a low-energy ($\sim$100 mJ) spark. The resulting weak shock wave is not nearly strong enough to ignite a detonation directly. It only causes multiple shock reflections and shock–flame interactions that distort and wrinkle the flame front.

Eqs. (2)–(8) are solved using an explicit, second-order, Godunov-type numerical scheme incorporating a Riemann solver. The integration is performed on a structured adaptive mesh based on the fully threaded tree data structure [44]. The mesh refinement is dynamically controlled by gradients of density, temperature, and composition. Typically, the maximum computational cell size (away from shocks and flame fronts) is $dx_{min} = 0.29$ cm, and the minimum refined cell size, $dx_{min} = 0.0163$ cm, which corresponds to 3–4 computational cells per laminar flame thickness.

Fig. 4 shows the one-dimensional flame structure calculated from a two-dimensional simulation of a planar flame propagating

Table 2
Model configurations.

Configuration*	7.6	17.4	52
L (cm)	216.2	1187.8	2130
d (cm)	7.6	17.4	52
ξ	1/3, 2/3	0.3, 0.6	0.3, 0.6
$x = l$ boundary	Closed	Open	Open
P_o(atm)	0.464	1	1
Experimental channel cross-section	Square	Circular	Circular
Experiments	[20]	[19]	[19]

* Note that tube diameter (for circular cross-sections) or side length (for square cross-sections) is used as a naming convention for each experiment.

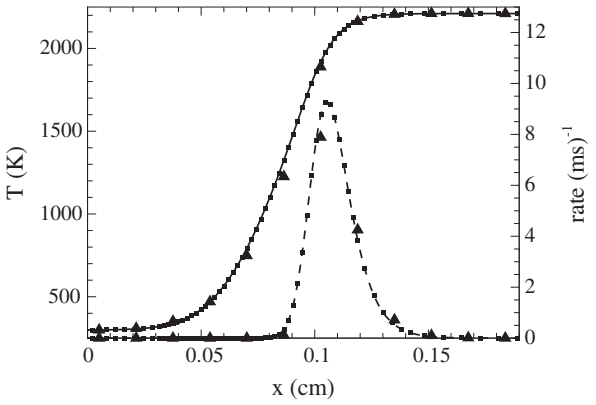

Fig. 4. Temperature (solid) and reaction-rate (dashed) profiles calculated using Eqs. (11), (12) (lines), two-dimensional Navier-Stokes equations with $dx_{min} = 0.018125$ cm (triangles), and the two-dimensional Navier-Stokes equations with $dx_{min} = 0.00113$ cm (squares).

in a smooth channel for this resolution (large symbols) and a finer resolution, $dx_{min} = 0.00113$ cm (small symbols). The flame structure calculated using the steady-state one-dimensional laminar flame model (Eqs. (11), (12)) is also shown in Fig. 4 (lines). The high-resolution two-dimensional calculation reproduces the theoretical flame structure and gives nearly the same flame speed. There are some differences in the reaction-rate profiles calculated at the lower resolution ($dx_{min} = 0.0163$ cm). The computed laminar flame speed is approximately 12% smaller than the theoretical laminar flame speed. More resolution tests are discussed in detail in Section 4.4. Here we only note that in larger channels, dx_{min} is limited by the available computational resources, and in most cases, the simulations must be somewhat under-resolved.

4.1. Configuration 7.6

Johansen and Ciccarelli [20] examined the development and acceleration of a turbulent flame in a 7.6×7.6 cm square cross-section channel. Obstacles, of heights 1.27, 1.9, and 2.53 cm corresponding to $\xi = 1/3$, 1/2, and 2/3, respectively, were spaced 7.6 cm apart over the entire 244 cm channel on both the top and bottom walls. Both ends of the chamber were closed, and the pressure of the stoichiometric methane–air mixture inside the chamber was initially 47 kPa. The mixture was ignited by an electric spark at the centerline of the channel.

We have simulated a two-dimensional rectangular channel (Fig. 3) with obstacle spacings and heights identical to those in the experiments. After ignition, we track the position and velocity of the leading edge of the flame front as well as the total length of flame surface created as the flame evolves. Flame velocities are computed at discrete locations along the length of the channel and represent an average velocity over the interval between two successive measurement locations. The flame surface is calculated by summing the total length of the isosurface on which $Y = 0.5$ at a particular instance in time. Fig. 5 compares measured [20] and computed flame velocities and flame surface areas for $\xi = 1/3$ and $\xi = 2/3$. At early times in the flame development, the simulations and experiments show similar flame velocities for both blockage ratios. Differences arise further downstream ($x \sim 100$–150 cm) as the flame evolves.

The flame acceleration process occurs in three phases, each of which can be characterized by the dominant mechanism driving the growth in flame surface area. In the first phase, the flame is folded and stretched by a laminar flow field that is induced by the thermal expansion of the combustion products.

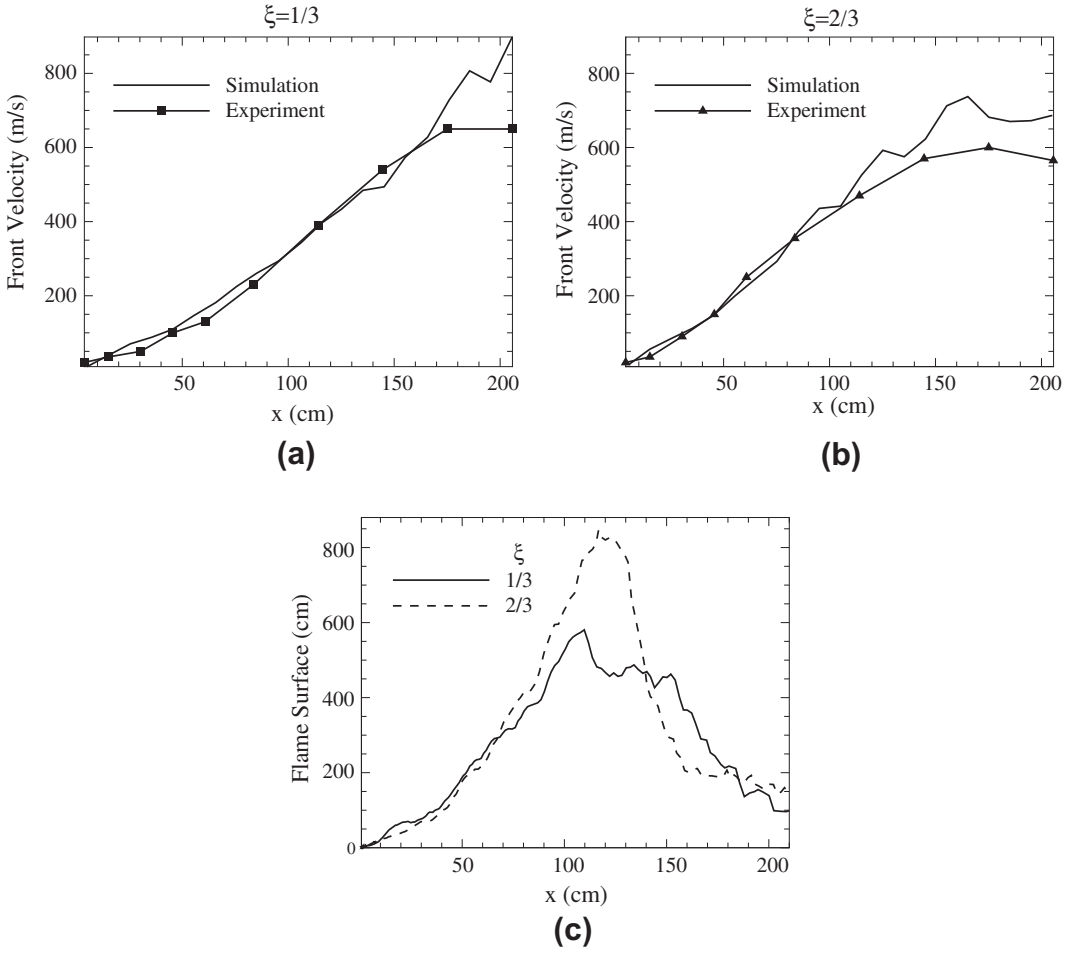

Fig. 5. Configuration 7.6: (a and b) Computed and measured [20] flame-propagation velocities and (c) computed flame-surface as a function of the position of the leading edge of the reaction front.

The development of flame surface is similar for $\xi = 1/3$ and 2/3 for this phase, $x \lesssim 70$ cm (Fig. 5c). Temperature maps of the leading edge of the flame as it passes over the first obstacle are shown in Fig. 6a and b. There is relatively little wrinkling of the flame front during this phase.

In the second phase, the predominant mechanism for increasing the total length of flame surface is wrinkling by fluid dynamic instabilities (e.g., Kelvin–Helmholtz and Rayleigh–Taylor) and turbulent fluctuations. Localized regions of vorticity stretch and fragment a continuous flame front, thereby increasing the total amount of flame-surface area. The energy released at the flame surface causes the thermal expansion of the product gases, which causes a net flow through the channel. Shear layers develop downstream of obstacles as the fluid is accelerated through the restricted cross-sectional area above them. Fluid dynamic instabilities and turbulence in the shear layers contribute to generation of more flame-surface area. The flame surface and velocity become substantially larger for the $\xi = 2/3$ case than for the $\xi = 1/3$ case for $x > 70$ cm. In the $\xi = 2/3$ case, the shear layers develop more quickly, since the flow is accelerated to a higher velocity in the smaller gap between obstacles.

It may be possible to describe the maximum turbulent flame speed attained during this stage of flame acceleration using a one-dimensional model, such as that described by Bradley et al. [45,46]; however, the turbulent flame brushes developed in our calculations are qualitatively different from the idealized one-dimensional turbulent flame. The extended burning regions between obstacles far behind the leading edge of the flame release significant amounts of energy, and in some regions the flame propagates normal to the direction of the induced gas flow.

Temperature maps of the flame fronts near $x = 100$ cm (Fig. 6c and d) show that there is much more small-scale flame structure and therefore much more flame surface in the $\xi = 2/3$ case. The increase in total flame-surface area (see Fig. 5c) continues as long as substantial amounts of fuel remain in between obstacles behind the foremost part of the flame front. Then, when most of this fuel is depleted, the amount of flame-surface decreases rapidly. The maximum flame-surface area developed for $\xi = 2/3$ is larger than that for $\xi = 1/3$ because the increased velocity of the flame front allows the flame to propagate farther in the channel before these extended reaction zones can burn out. The extra amount of flame surface present in these regions results in faster depletion of the fuel, and hence the steep drop in flame-surface area for $x \gtrsim 130$ cm.

This rapid decline in flame-surface area is slowed as the flame enters the third phase. When the speed of the induced flow approaches the speed of sound in the unburned mixture ahead of the flame, energy released at the leading edge of the flame front generates weak pressure waves that propagate ahead of the flame. These pressure waves later become shocks, which can reflect from obstacles and walls. The reflected shocks also collide and interact with portions of the reaction front. The flame surface is wrinkled by these shock–flame interactions that promote Richtmyer–Meshkov instabilities. The turbulence generated by these instabilities is

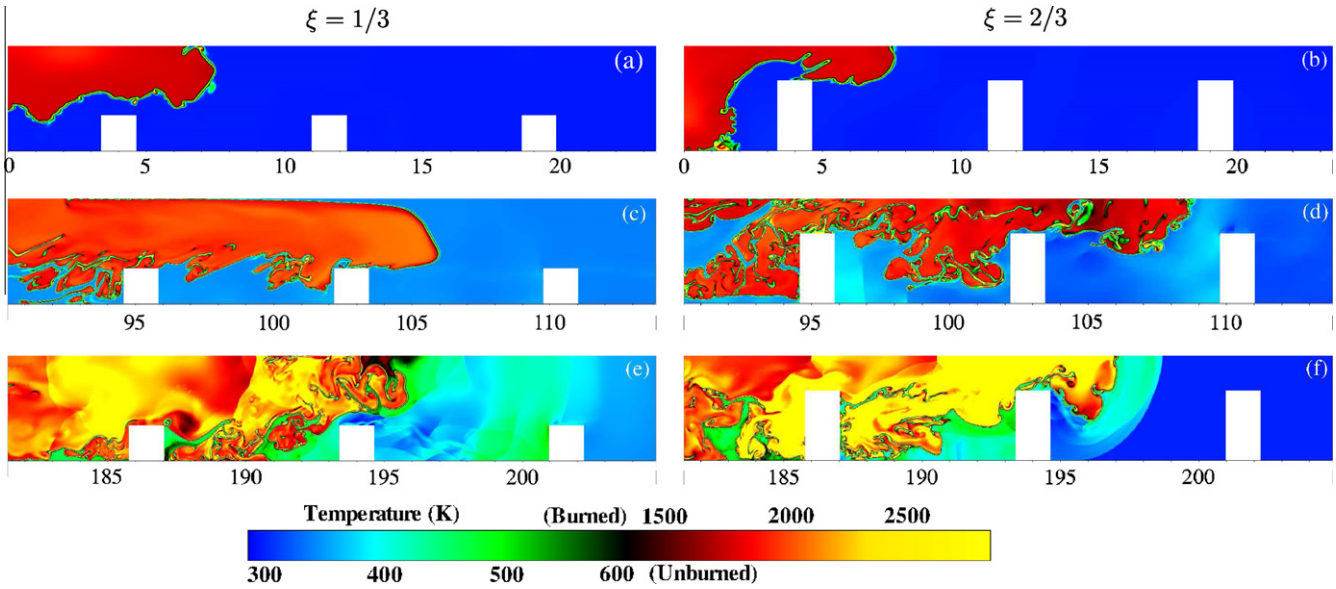

Fig. 6. Temperature maps near the leading edge of the flame for configuration 7.6 with $\xi = 1/3$ (left) and $\xi = 2/3$ (right) at several locations throughout the channel: (a and b) near first obstacle, (c and d) near $x = 100$ cm, and (e and f) near $x = 200$ cm. The top temperature scale is for burned material, and the bottom scale is for unburned material. Time increases from top to bottom in each column.

not, necessarily, homogeneous, isotropic, Kolmogorov turbulence. The nature of this turbulence and its interaction with the flame are interesting areas of future investigation. Here, the additional energy release caused by flame-surface wrinkling helps to sustain the flame speed and slow the decline in the net flame surface. This process occurs for $x \gtrsim 160$ cm for $\xi = 2/3$, but does not begin to occur in the $\xi = 1/3$ case until the flame reaches the end of the domain. A longer channel would be necessary to observe significant shock–flame interactions for the $\xi = 1/3$ case. Fig. 6e and f compare the temperature maps for $\xi = 1/3$ and 2/3 when the leading edge of the flame is near $x = 200$ cm. A well-defined shock wave has formed in the $\xi = 2/3$ case, but the waves ahead of the flame front have not yet coalesced into a shock for $\xi = 1/3$.

4.2. Configurations 17.4 and 52

Kuznetsov et al. [19] performed similar experiments in circular cross-section tubes with diameters of 17.4 cm and 52.0 cm. The obstacles in the tubes were annular orifice plates that were spaced one diameter apart. The blockage ratio defined in these experiments is then $\xi^* = 1 - (D^*/D)^2$, where D and D^* are the tube diameter and orifice diameter, respectively. In these experiments, one end of the tube was left open to the atmosphere, and the initial gas pressure was atmospheric throughout the tube. They ignited the uniform stoichiometric methane–air mixture near the tube axis at the closed end. Photodiodes were placed at various positions along the walls of the tubes, and reaction-front velocities were calculated based on time-of-arrival measurements.

After the initial acceleration period, two propagation velocity regimes were found. The first, commonly referred to as the "choking" regime, is characterized by a velocity close to $1/2D_{CJ}$ [47]. The second regime, the "quasi-detonation," is characterized by a flame-front velocity just less than D_{CJ}. For a blockage ratio of $\xi^* = 0.3$, the experimentally measured flame speed fluctuates between the speeds typical of these two propagation regimes. This indicates that the 17.4 cm diameter tube is close to the critical size for detonation propagation, as supported by the observation that $D/\lambda < 1$ for the stoichiometric methane–air system. For the larger blockage ratio, $\xi^* = 0.6$, the experimental flame velocity approaches a steady value of approximately 700 m/s, a velocity characteristic of the choking propagation regime. Similar results were obtained for the $D = 52.0$ cm tube.

We performed simulations similar to these experiments using the configuration shown in Fig. 3 with $d = D$ and $\xi = \xi^*$ for both the 17.4 cm (configuration 17.4) and 52 cm (configuration 52) cases. Because of the differences in geometry, the obstacle heights in the simulations, h, are slightly larger than the heights of the orifice plates in the experiments, $h^* = (D - D^*)/2$, for the same blockage ratios. Fig. 7 shows the calculated flame velocities and surface areas for configuration 17.4 as a function of the position of the leading edge of the reaction wave for $\xi = 0.3$ and 0.6. The symbols on Fig. 7a,b are flame-velocity data from the experiments in the 17.4 cm tubes [19]. In both the calculations and experiments, the flame accelerates to a fixed velocity characteristic of the choking regime, which then either undergoes DDT or continues to propagate at this average speed. The initial flame acceleration is similar to that described in the previous section: flames are stretched by the thermal-expansion-induced flow, wrinkled and torn by turbulence and fluid dynamic instabilities, and further fragmented by shock–flame interactions. For example, the black line in each frame in Fig. 8 shows the progress of a shock colliding with and passing through a flame. As the shock passes through, significantly more flame-surface area is created behind it. For the cases shown in Fig. 7, the channel is long enough for the flames to progress through all three stages of the acceleration process.

The evolution of flame surfaces for $0 < x \lesssim 450$ cm shown in Fig. 7c follows the same trend as in the early stages of configuration 7.6. For $x \gtrsim 450$ cm and $\xi = 0.3$, the flame-surface area sharply decreases. At this point, however, the reaction-front velocity jumps to D_{CJ}, indicating that a detonation was initiated and survived. The sequence of events that lead to DDT is shown in Fig. 9a–e. Strong shock waves formed ahead of the flame front reflect off of the channel wall and the faces of obstacles, which results in even stronger waves and more shock–flame interactions. Eventually, Mach stems form and these raise the local temperature close to the ignition point. These regions of elevated temperature, or hot spots, may or may not ignite, depending on the ignition delay time of the mixture and the length of time the temperature remains elevated. The hot spot created by a Mach stem just beginning to reflect from the base of the obstacle in Fig. 9b (at

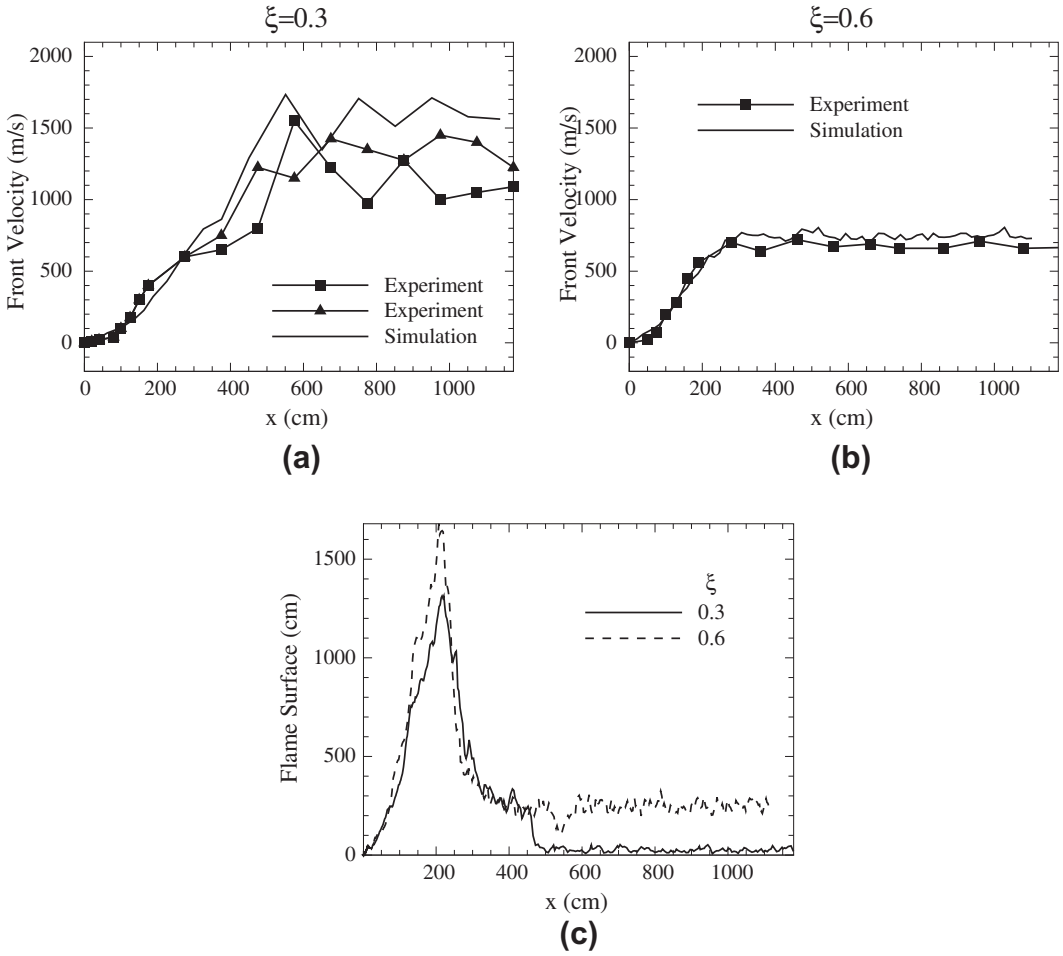

Fig. 7. Configuration 17.4: (a and b) Reaction front-propagation velocities and (c) calculated flame-surface lengths as a function of the position of the leading edge of the reaction front.

450 cm) leads to a successful detonation ignition. The detonation then propagates into unburned fuel, catches up to the leading shock wave, and proceeds to consume nearly all unburnt fuel in that region (Fig. 9c–e). This is qualitatively similar to the process reported for detonation ignition in hydrogen–oxygen mixtures in channels with obstacles [16,17]. The size of the system, however, is considerably larger for the methane–air mixture.

The velocity curves shown in Fig. 7a for $d = 17.4$ cm and $\xi = 0.3$ indicate that the detonation propagates at a speed much less than D_{CJ}. This is a result of recurring detonation diffractions that continually decouple the flame from the leading shock. The detonation is then reignited at a subsequent obstacle in the manner discussed above. Although a detonation propagates at a speed greater than or equal to D_{CJ}, a fast deglagration (decoupled flame and shock) propagates significantly slower. Thus, the time-averaged velocity for this quasi-detonation, characterized by intermittent periods of detonation and fast deflagration propagation, is below D_{CJ}. An example of detonation failure and subsequent reignition is shown in Fig. 9e–j. This repeated ignition and decoupling process leads to the observed smaller propagation velocities for this case.

The velocities obtained for the $d = 52$ cm cases ($\xi = 0.3$ and 0.6) are shown in Fig. 10. For $\xi = 0.3$, the computed and measured [19] flame velocities are very similar during the initial flame acceleration period ($x \lesssim 700$ cm). Near 700 cm, DDT occurs in the simulated system and the computed velocity jumps to $\sim$1800 m/s. This propagation speed is much closer to D_{CJ} than that observed in configuration 17.4, $\xi = 0.3$ since fewer instances of shock–flame decoupling take place in the larger channel. In the experiments, DDT first occurs farther downstream, near $x \sim 1000$ cm, and the quasi-detonation velocity is somewhat smaller than the calculated value. For $\xi = 0.6$, the computed flame acceleration is close to the experimental data. In the simulations, several instances of DDT were observed, while no DDT occurred in the experiments. The total flame surface for the $\xi = 0.6$ simulation is everywhere greater than that of the $\xi = 0.3$ simulation. Larger pockets of unburned fuel between obstacles take longer to burn and delay the onset of the rapid decline in flame-surface area that occurred in configurations 7.6 and 17.4 for the larger blockage ratios. By the time the pockets of fuel begin to burn out, the leading edge of the propagating flame has already accelerated to the point where frequent shock–flame interactions significantly increase the amount of flame surface, leading to less rapid net losses of flame-surface area.

The detonation is less likely to fail when the orifice diameter, D^*, is large compared to the detonation cell size. Peraldi et al. [30] suggested that a suitable criterion for whether or not DDT can occur in obstructed channels is $D^*/\lambda > 1$. Dorofeev et al. [48] proposed a different metric based on a length scale that depends on the distance between the leading edges of adjacent obstacles, S, (cf. Fig. 3) and the orifice diameter. They showed that the metric $L^*/\lambda > 7$, where $L^* = (S + D)/2/(1 - D^*/D)$ was a reliable indicator. Table 3 shows approximate values for D^*/λ and L^*/λ for each of the experimental systems.

For the 52 cm tube with $\xi = 0.3$, D^*/λ and L^*/λ are both much larger than the critical values. The experimental data show that DDT

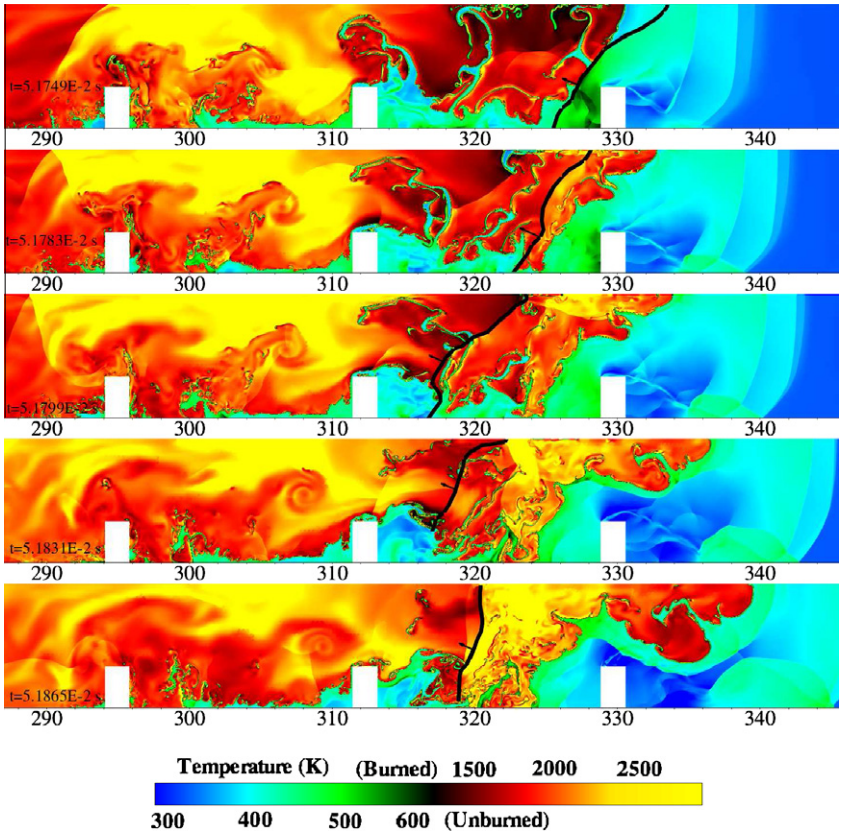

Fig. 8. Temperature maps near the leading edge of flame in configuration 17.4 with $\xi = 0.3$ as a shock interacts with the flame front. The heavy black line indicates the location of a shock, and the arrow indicates the direction of propagation. The top temperature scale is for burned material, and the bottom scale is for unburned material. Time increases from top to bottom.

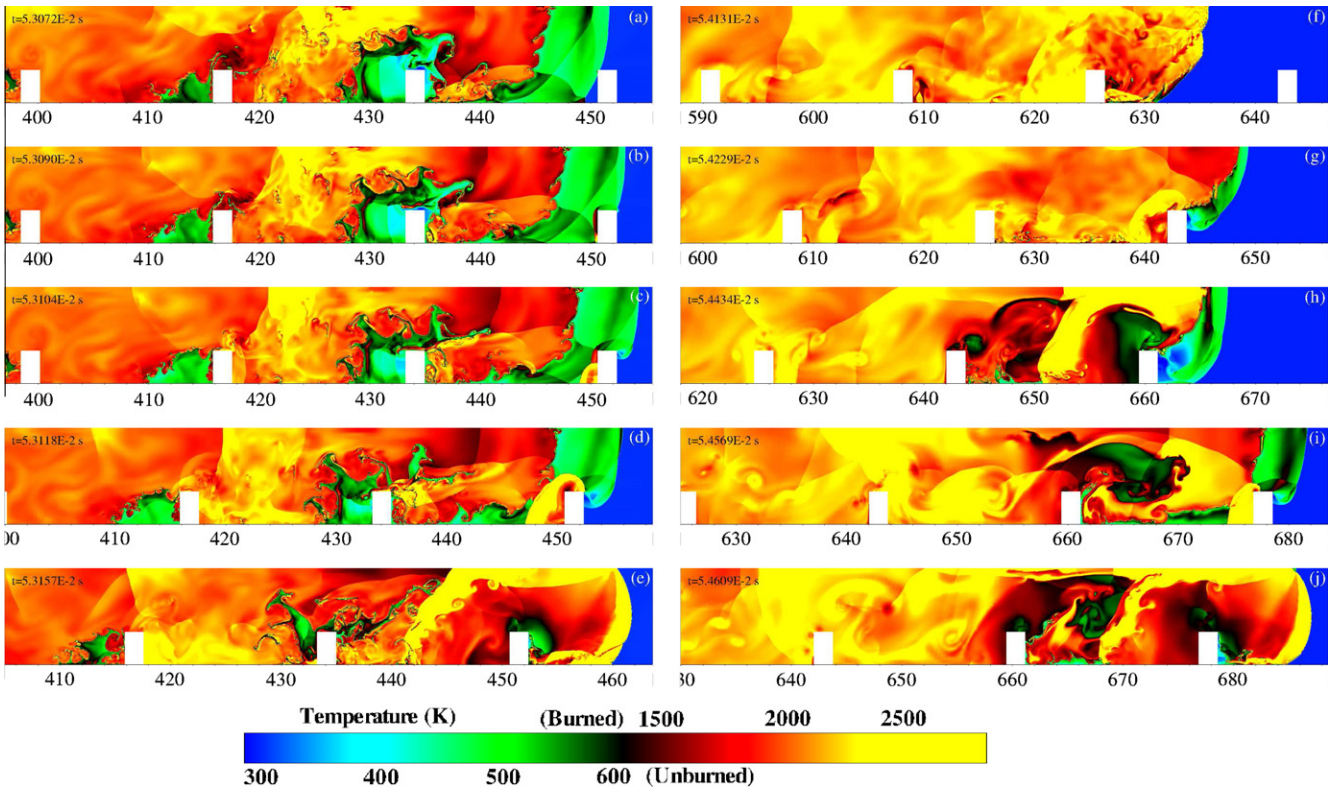

Fig. 9. Configuration 17.4, $\xi = 0.3$: Temperature maps near the leading edge of the reaction front that show DDT (left column) and shock–flame decoupling followed by subsequent detonation reignition (right column). The top temperature scale is for burned material, and the bottom scale is for unburned material. Time increases in alphabetical order in panels (a) through (j).

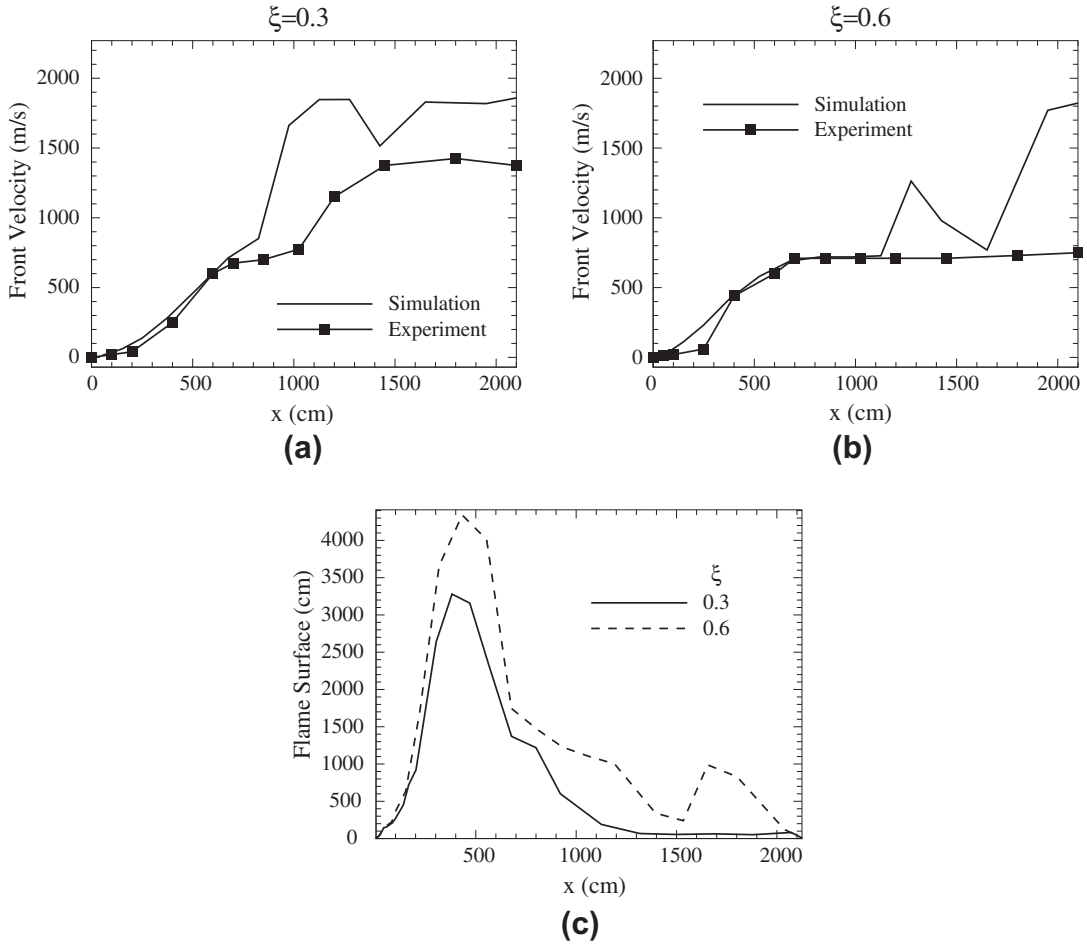

Fig. 10. Configuration 52: (a and b) Reaction front-propagation velocities and (c) calculated flame-surface lengths as a function of the position of the leading edge of the reaction front.

Table 3
Values of DDT criterion proposed by Peraldi et al. [30] and Dorofeev et al. [48] for the experimental systems [19] and the model configurations used in the simulations.

ξ	Experiments				Simulations			
	D (cm)	D^*/λ	L^*/λ	DDT?	d (cm)	D'/λ	L'/λ	DDT?
0.3	17.4	0.75	5.6	Yes	17.4	0.6	3	Yes
	52	2.25	17	Yes	52	1.9	9	Yes
0.6	17.4	0.6	2.5	No	17.4	0.4	1.5	No
	52	1.7	7	No	52	1.1	4.5	Yes

occurred (Fig. 10a), but the propagation velocity was lower than D_{CJ} and consistent with the quasi-detonation velocity of between 1400 and 1500 m/s. When $\xi = 0.6$ for the 52 cm tube, DDT should occur based on the D^*/λ criterion, but the L^*/λ criterion suggests that the system is near the critical value. The experiments show that DDT did not occur for this case (Fig. 10b).

For the $D = 17.4$ cm tube, all of the criteria are less than their critical values (Table 3), yet there is some indication of DDT in the experimental data for $\xi = 0.3$ (Fig. 7a). In this case, the propagation velocity alternates between quasi-detonation and choking, indicating long periods of propagation as a fast deflagration between shorter periods of detonation propagation.

In the simulations, the orifice size $D' = d - 2h$ is always smaller than D^* in the experiments when $d = D$ and $\xi^* = \xi$. Accordingly, D'/λ and L'/λ, where $L' = d/(1 - D'/d)$, are also smaller than D^*/λ and L^*/λ. Based on criteria $D'/\lambda > 1$ and $L'/\lambda > 7$ and assuming, for the moment, that the characteristic λ for the simulations is the same as that for the experiments ($\lambda = 19$ cm), the only case that should be expected to undergo DDT is configuration 52 with $\xi = 0.3$. Fig. 10a does show DDT for this case, and the resulting propagation velocity is larger than the experimental data. The velocity data from configuration 52 with $\xi = 0.6$ also show occasional transitions to detonation, but the average propagation speed is much smaller than that obtained in the case of smaller blockage ratio. For configuration 17.4, DDT occurs in the $\xi = 0.3$ case in spite of the low values of D'/λ and L'/λ.

The simulation data suggest that the transition criteria $D'/\lambda > 1$ and $L'/\lambda > 7$ may not be sufficient to predict whether or not DDT will occur in the systems under consideration. Transitions to detonations were found for D'/λ and L'/λ as low as 0.6 and 3, respectively; however, some care must be taken when evaluating these transition criteria. First, detonation cells in methane–air mixtures are highly irregular structures, so the specification of an average λ has large uncertainties, thus making it difficult to compare the sizes of measured and calculated detonation cells. It is possible that the characteristic size of the simulated λ is smaller than that used in computing the ratios, which would have the effect of increasing D'/λ and L'/λ for each simulation. Second, the differences in geometry between the simulations and experiments, particularly the differences in obstacle heights, could produce different shock reflections, and this can affect the occurrence, time, and location of DDT. Given these differences, there is no reason to expect that the critical values of the empirical transition criteria for tubes will be the same as those for a two-dimensional channel. Any further consideration of the matter would require a detailed study of the

cellular structure of stoichiometric methane–air detonations in order to obtain a truly reliable estimate of the average cell size.

4.3. Sensitivity analysis

It is important to evaluate the sensitivity of the computed flame acceleration and occurrences of DDT to variations in the parameters of the chemistry model. We first consider the sensitivity of the flame acceleration by evaluating how much velocity profiles change when there are systematic variations in the length and time scales of the laminar flame. This is done by changing model parameters A, q, E_a, and γ to create moderate (10–15%) variations in the laminar flame velocity, adiabatic flame temperature, and specific-heat ratio. We next consider the impact on DDT of changing these parameters. As discussed earlier, model parameters also affect various length and time scales of detonation waves, in particular, D_{CJ}, λ, and ignition delay times.

The first question to address is how changes in model parameters affect the propagation velocity of the flame in an obstructed channel. We performed a series of simulations using configuration 17.4 with $\xi = 0.3$ and *0.6*. Fig. 11 shows the velocity of the leading edge of the flame front as a function of position. In Fig. 11a, we consider several different sets of parameters that yield the same $T_b = 2210$ K but different values of the one-dimensional laminar flame speed. A description of each parameter set, $\mathscr{P}$, is given in Table 4 along with the corresponding laminar flame and 1D detonation properties calculated from Eqs. (11)–(16). The solid lines represent calculations for a parameter set $\mathscr{P}1$ that gives $S_l = 38.02$ cm/s, while the laminar burning velocity of the flames represented by the dashed ($\mathscr{P}2$) and dotted ($\mathscr{P}3$) lines is 32.5 cm/s. In $\mathscr{P}2$, the decrease in S_l was caused by reducing A to 1.2×10^{13} cm^3/g s. In $\mathscr{P}3$, the same reduction in S_l was brought about by increasing the activation energy to $E_a = 69.45RT_0$ for the same A used in $\mathscr{P}1$. The results were nearly identical for all three

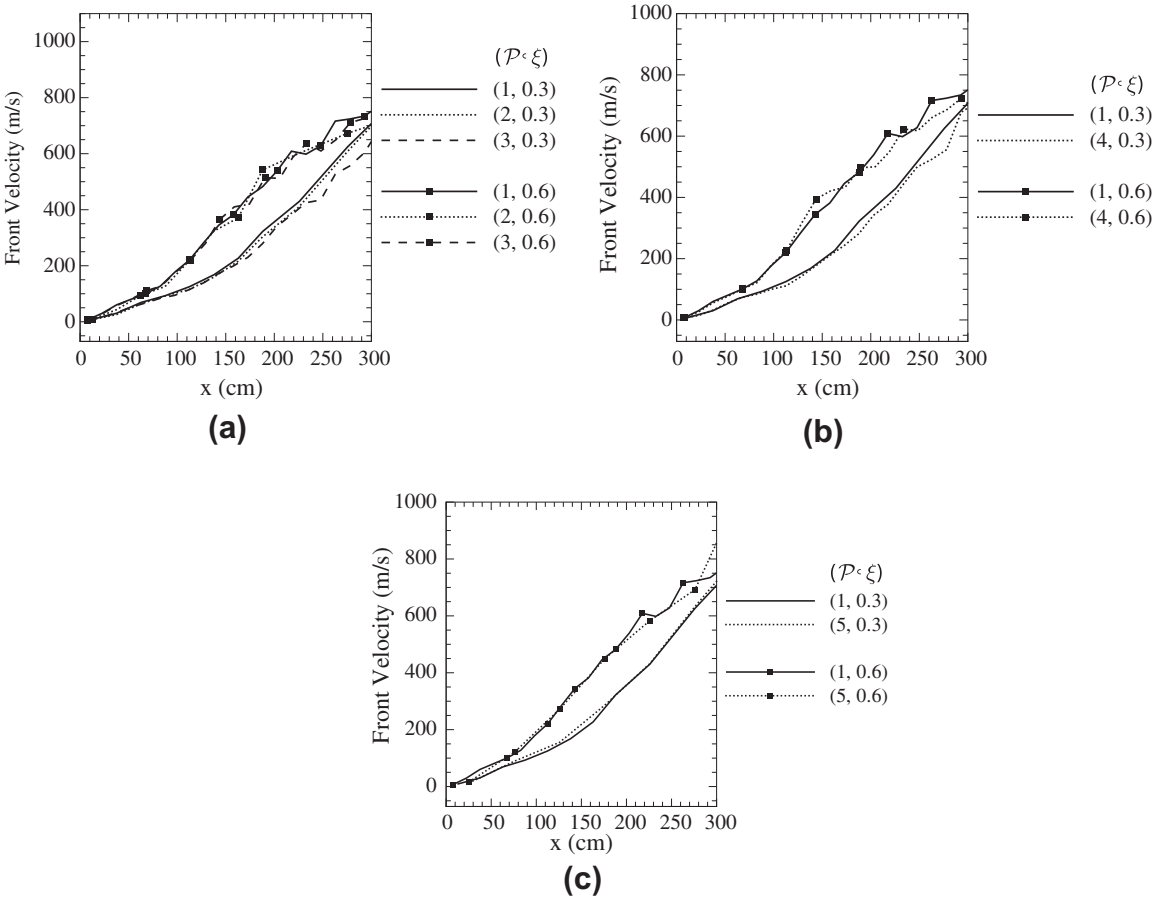

Fig. 11. Reaction front-propagation velocities as a function of the position of the leading edge of the reaction front for $x < 300$ cm in configuration 17.4 calculated using parameter sets, $\mathscr{P}$, (a) 1, 2, 3, (b) 1, 4, and (c) 1, 5. See Table 4 for descriptions of the parameter sets. Lines with symbols represent $\xi = 0.6$, and those without represent $\xi = 0.3$.

Table 4
Parameter sets used in Figs.11 and 12 and their corresponding laminar flame and one-dimensional detonation properties.

$\mathscr{P}$	1	2	3	4	5
A (cm^3/g s)	1.64×10^{13}	1.2×10^{13}	1.64×10^{13}	4.411×10^{13}	1.64×10^{13}
E_a/RT_0	67.55	67.55	69.45	67.55	67.55
qM/RT_0	39.0	39.0	39.0	34.71	34.82
γ	1.197	1.197	1.197	1.197	1.226
S_l (cm/s)	38.02	32.0	32.0	38.02	38.02
T_b (K)	2210	2210	2210	2000	2210
D_{CJ} (m/s)	1820	1820	1820	1724	1854
x_d (cm)	0.229	0.331	0.356	0.332	0.0616

cases with $\xi = 0.6$, and only slight differences between $\mathscr{P}3$ and $\mathscr{P}1$ were found later in the flame development ($x \gtrsim 250$ cm) for $\xi = 0.3$. These simulations suggest that, in the range of S_l considered, it has negligible influence on the evolution of the flame propagation speed in the channel.

The effect of the adiabatic flame temperature on the flame acceleration was tested by changing the amount of heat released per unit mass of fuel, while maintaining a constant S_l. This was done by inversely changing q and A. Reducing q has the effect of lowering both S_l and T_b, but a change in A affects only S_l. Thus, the procedure is to set $q = (T_b - T_o)/c_p$ for the desired T_b, and then to choose A such that the laminar flame speed calculated using the one-dimensional flame model discussed in the previous section is equal to the desired S_l. Parameter set $\mathscr{P}4$ yields cooler flames ($T_b = 2000$ K) for the same $S_l = 38.02$ cm/s as $\mathscr{P}1$. Fig. 11b shows the flame acceleration obtained using these two parameter sets for $\xi = 0.3$ and 0.6. Again, the results obtained suggest this temperature difference has no noticeable effect on flame acceleration.

The effect of varying γ (and, hence, the sound speed) on the flame acceleration is shown in Fig. 11c. Two sets of parameters that give equal S_l and T_b but different ratios of specific heat are considered. In the first ($\mathscr{P}1$), we use $\gamma = 1.197$. In the second set, we use $\gamma = 1.226$ and decrease q to $34.82RT_o/M$ to maintain $T_b = 2210$ K. The values of E_a and A are unchanged compared to $\mathscr{P}1$, so S_l is also the same 38.02 cm/s. Only slight differences between the two cases are noticeable for both $\xi = 0.3$ and 0.6.

The second important issue is how the choice of model parameters affects the onset of the DDT. We note here that it is difficult to treat this issue in a truly quantitative manner because DDT is a stochastic process that depends on the formation of relatively small hot spots, and these result from combinations of shock reflections or turbulent fluctuations. In some situations, even seemingly imperceptible changes in any physical or numerical parameters or background conditions can lead to significant random variations of distances or times to detonation initiation [16]. Even with these caveats, we should still be able to get a qualitative idea of the likelihood of DDT for a given parameter set. Fig. 12 shows the reaction-front velocities in the downstream section of the channels for the cases shown in Fig. 11.

For the cases shown in Fig. 12a, a reduction in A or an increase in E_a leads to an increase in x_d (and λ) and, hence, smaller D'/λ and L'/λ. When these ratios are small, detonations are less likely to be able to propagate through the smaller space above an obstacle. When a detonation fails, the reaction zone decouples from the leading shock wave and propagates at a speed much smaller than D_C. The length of time the reaction front spends propagating as a detonation is thus reduced, lowering the average propagation speed of the reaction wave. This may account for the slightly lower average reaction-front velocities in the quasi-detonation regime (dotted and dashed lines) shown in Fig. 12a for $\xi = 0.3$. A reduction in A or an increase in E_a also increases induction times behind shocks, and this can delay the detonation initiation. Fig. 12a shows, however, that the onset of DDT occurs later for smaller A, but sooner for larger E_a. A more comprehensive parametric study would be required to determine conclusively whether this result is attributable to the systematic variation in parameters. For $\xi = 0.6$, the reac-

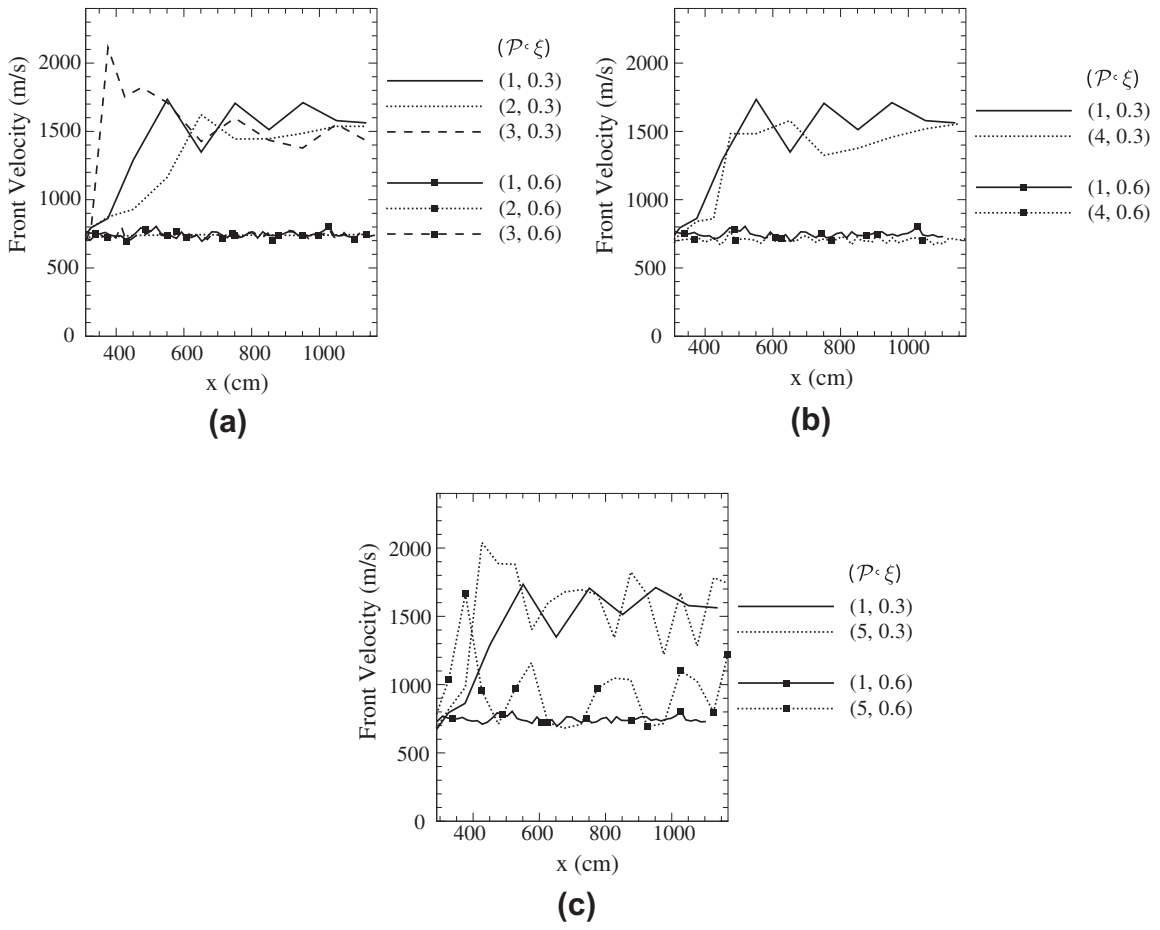

Fig. 12. Reaction front-propagation velocities as a function of the position of the leading edge of the reaction front for $x > 300$ cm in configuration 17.4 calculated using parameter sets, $\mathscr{P}$, (a) 1, 2, 3, (b) 1, 4, and (c) 1, 5. See Table 4 for descriptions of the parameter sets. Lines with symbols represent $\xi = 0.6$, and those without represent $\xi = 0.3$.

tion fronts propagate at the choking velocity, and all three $\mathscr{P}$ give essentially the same propagation speed.

Fig. 12b shows the effect of simultaneously decreasing q and increasing A. For laminar flames, this procedure lowers the adiabatic flame temperature while maintaining constant S_l. For detonations, varying the parameters in this way has the effect of decreasing D_{CJ} and increasing x_d and λ. The change in λ caused by the change in model parameters is not sufficient to drop D'/λ or L'/λ below their critical values for the $\xi = 0.3$ case, however. The small effect on computed distances to DDT is also consistent with the fact that induction delays, which are inversely proportional to qA, are not significantly affected. The quasi-detonation propagation velocity for the ($\mathscr{P}4$, $\xi = 0.3$) case is also less than the result shown for $\mathscr{P}2$ in Fig. 12a for which the values of x_d are similar. The difference in the propagation velocity is likely caused by the lower D_{CJ} attained using $\mathscr{P}4$. Once again the results are similar for the $\xi = 0.6$ cases, where the reaction fronts propagate at the choking velocity. The reaction wave generated using $\mathscr{P}4$ propagates slightly slower than that generated using $\mathscr{P}1$ because the temperature (and, hence, sound speed) in the combustion products is lower.

The choice of γ (more precisely, $\gamma - 1$) plays a large role in detonation initiation and propagation. Using $\mathscr{P}5$, we investigate how increasing $\gamma - 1$ by 15% (so that $\gamma = 1.226$) affects the transition to detonation. As discussed earlier, in $\mathscr{P}5$ a smaller value of q is used so that the computed S_l and T_b are the same as those computed for $\mathscr{P}1$ and recorded in Table 1. The average reaction-front velocities computed using $\mathscr{P}5$ and $\mathscr{P}1$ are shown in Fig. 12c. For the larger-γ simulations, shock dynamics and post-shock temperatures changed in the way that reduced induction delays behind shocks. This is probably the main reason why DDT occured sooner for the $\xi = 0.3$ case, and now even appeared for the $\xi = 0.6$ case. The computed value of D_{CJ} was only about 1.8% larger than that of stoichiometric methane–air mixtures (cf. Table 1), but x_d was 3.7 times smaller than that computed for $\gamma = 1.197$. For $\xi = 0.3$, the detonation propagates as a quasi-detonation in a manner similar to that observed using set $\mathscr{P}1$. For $\xi = 0.6$ and large γ, we see several instances of detonation initiation and failure, which is not surprising since the new $D'/\lambda = 1.5$ or $L'/\lambda = 5.6$ are much closer to their critical values discussed in the preceding section. The transitions are infrequent, and the average propagation velocity is smaller than D_{CJ} and the quasi-detonation propagation velocities observed for the $\xi = 0.3$ cases.

The results shown in Figs. 11, 12 indicate that varying the model parameters to result in relatively small (10–15%) changes in individual laminar flame properties has little impact on the observed flame acceleration. In general, the effects on DDT are also small. It is not clear whether the differences in the first occurrence of DDT among the several parameter sets shown in Fig. 12a are due to physical differences in the modeled systems or to chance fluctuations in the thermodynamic conditions within the hot spots that initiate detonations. The changes in model parameters for $\mathscr{P}2$ and $\mathscr{P}3$ both have the effect of increasing induction times behind shocks (an effect that could delay DDT), but the resulting first occurrences of DDT appeared later and sooner than the baseline case, respectively. Small changes in the thickness of the detonation wave (and detonation cell size) result in correspondingly small changes in the average propagation velocity and first occurrences of DDT unless the system is near a critical value for detonation propagation. In such a system, even a small increase in detonation cell size could impede DDT. In systems sufficiently larger or smaller than the critical size for DDT for a given fuel mixture, the interaction of the induced flow and shocks with the wrinkled flame surface seems to have a much larger influence on the large-scale behavior of the reaction front than the details of the model chemistry in these types of obstructed channels.

There are other physical properties of the gas mixture that have not been discussed here that could potentially impact the first occurrence of DDT. For instance, the ratio of the acoustic time in the Zeldovich reactivity gradient to the reaction time [49] has been shown to be relevant to the development of a detonation [50]. It is not possible to vary the reaction time and the induction time independently using a one-step reaction model. This could be done with a multiple-step reaction model, but at a higher computational cost. Evaluating whether solutions obtained using a multiple-step reaction model would produce more accurate results and, if so, whether the improvement justifies the additional computational costs is left for future investigations.

4.4. Flame resolution tests

The issue of how much grid resolution is necessary at the reaction front becomes extremely important when attempting to simulate flame acceleration and DDT for very large-scale explosions. The size of the system that can be simulated will be limited by the number of refined cells required to obtain a sufficiently accurate description of the reacting flow. Thus, it is useful to know the largest cell size that can be used to meet this requirement. We tested the effect of the reaction front resolution on flame acceleration in configuration 7.6 with $\xi = 1/3$ using the model parameters shown in Table 1. In all cases, the flame is initiated from a spark of size $r_f = 0.25$ cm. Three values of dx_{min} were tested, 0.018124 cm (corresponding to ~3 computational cells per laminar flame thickness), 0.009062 cm (~5 cells/flame thickness), and 0.004531 cm (~10 cells/flame thickness). Fig. 13a shows the prop-

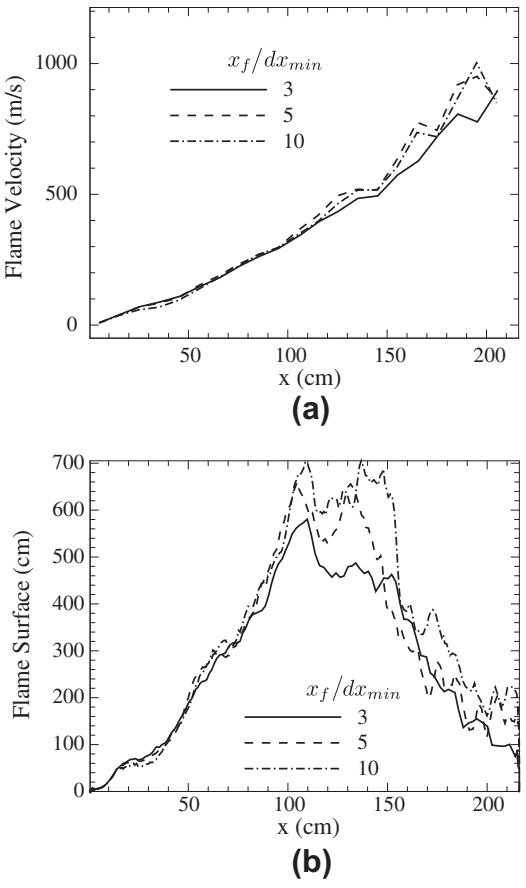

Fig. 13. (a) Flame velocity and (b) flame-surface length as a function of position of leading edge of a flame for configuration 7.6, $\xi = 1/3$ using three successively more-refined grid resolutions.

agation velocity of the leading edge of the flame, and Fig. 13b shows the development of the flame surface, both as a function of the position of the leading edge of the flame. As the minimum grid size is decreased, and the flame front becomes more resolved, the peak amount of flame surface increases. The computed flame velocity during the later stages of the flame acceleration process increases as well when the number of grid cells in the reaction zone is increased from 3 to 5. A subsequent increase from 5 cells to 10 cells has little impact on the bulk acceleration of the flame.

5. Summary and conclusions

In this work, we have calculated DDT in stoichiometric mixtures of methane and air in channels with obstacles. The systems simulated are too large to compute with a detailed, multistep, multispecies chemical reaction mechanism, and there is no simple, inexpensive reduced mechanism that can be used for both flames and detonations. Thus, we developed and calibrated a single-step reaction-diffusion model that correctly reproduces the length and time scales of both laminar flames and detonations, yet is computationally efficient enough to use in large-scale computations. The computed velocities of the reaction fronts as the flames accelerated and transitioned to detonations showed reasonable qualitative and quantitative agreement to those measured in experiments of similar sizes and geometries. The comparison is good enough to give us confidence in using the model.

Three stages of flame acceleration were observed: flame stretching and folding, flame-front wrinkling caused by turbulent eddies and fluid-dynamic instabilities, and flame-surface creation by shock–flame interactions. Higher levels of flame-surface wrinkling cause the flame to accelerate more rapidly, but the final choking velocity is the same for all geometric configurations and depends only on properties of the gas mixture. Transitions to detonation are observed in systems where Dorofeev's criterium $L^* = (S + D)/2/(1 - D^*/D)$ was large compared to the detonation cell size. Detonations appear when shock reflections from channel walls and obstacles locally raise the temperature in the unburned gases to the ignition point. This initiates a reaction that can ignite a detonation by Zeldovich's gradient mechanism. The survival of the detonation then depends on the local thermodynamic conditions and the size of the orifice through which it will propagate. Frequent detonation failure and reignition lowers the average detonation velocities to below D_{CJ}, which is consistent with experimental evidence.

We showed that the large-scale flame dynamics and DDT are generally insensitive to small changes in model parameters. Only relatively minor differences in the acceleration of the flames were observed for 10–15% variations in the laminar flame speed, adiabatic flame temperature, and specific-heat ratio. The distances to DDT showed a somewhat wider variation for different parameter sets. The most likely explanation for this is the dependence of ignition delay times behind shocks on the model parameters. Reflected shocks and Mach stems are more likely to be able to ignite a detonation when the ignition delays are short, but whether or not this occurs at a particular location is highly dependent on the system geometry and stochastic variations of local thermodynamic conditions. This makes the exact prediction of the location of DDT extremely difficult. Definitively separating the effect of the model parameters on DDT from the effects of stochasticity would require a more comprehensive study and is left for future work.

The parameter that has the most pronounced effect on DDT is the specific heat ratio. The value of γ determines post-shock temperatures and pressures, which strongly influence the detonation structure. A 15% change in $\gamma - 1$ was found to decrease the width of a 1D detonation by a factor of 3. For the systems considered, this change affected the distance to DDT for $\xi = 0.3$ and the ability of a detonation to form when $\xi = 0.6$. The strong dependence of detonation structure on γ makes the choice of this parameter important for the simulations. A future area of investigation would be to see how using a temperature-dependent γ would affect shock–flame interactions and DDT.

A series of grid resolution tests showed that increasing the resolution from 5 to 10 cells per laminar flame thickness has practically no effect on the flame acceleration. Small differences in the flame speed found for under-resolved reaction zones (3 cells per laminar flame thickness) have only a minor impact on the large-scale flame development.

In spite of geometrical differences between the model configurations used in the simulations and the experimental systems to which they are compared, we observed reasonable agreement in flame development and DDT. Such quantitative agreement between 2D simulations and 3D experiments may seem strange since the difference in the equilibrium energy cascade for two-dimensional and three-dimensional turbulence is substantial. It has been suggested, however, that in flows where repeated shock–flame interactions drive the fluid instabilities, the turbulence is nonequilibrium and that energy is transferred directly into a broad range of scales simultaneously (see, e.g., [15]). Under this paradigm, different scales of turbulent motion are populated more efficiently than through the standard Kolmogorov energy cascade model. In our simulations, shock–flame interactions become important as the velocity of the leading edge of the flame approaches the speed of sound in the burned material and play a large role in the final stage of the flame acceleration process.

DDT in our simulations occurs due to the appearance of hot spots behind a shock wave or Mach stem. Whether or not these hot spots can trigger a detonation depends on the strength of the shock. We found that the critical system sizes for DDT in our calculations were smaller than those in the experiments. The level of uncertainty inherent in the determination of average detonation cell sizes in methane–air mixtures, however, precludes us from making a quantitative assessment of DDT criteria.

Acknowledgments

This work was supported by the National Institute for Occupational Safety and Health (NIOSH) and the Naval Research Laboratory (NRL) through the Office of Naval Research. Computational facilities were provided by the Laboratory for Computational Physics and Fluid Dynamics and the DoD High Performance Computing Modernization Project. The authors thank R. Karl Zipf, Michael Sapko, Khaled Mohamed, Walter Marchewka, James Addis, Frank Karnack, and Eric Weiss of NIOSH for many engaging discussions concerning methane–air explosions and Alexei Poludnenko for several discussions concerning the nature of turbulence in shock-laden flows. The authors also thank an anonymous reviewer for several insightful comments during the review process.

Appendix A. 1D Steady-state flame

We assume that the Lewis number of the fuel mixture is unity, which gives Y as a linear function of temperature,

$$Y = 1 - (T - T_o)C_p/q, \tag{A.1}$$

so that the the reaction rate becomes a function of temperature only, $\Omega = A(1 - (T - T_o)C_p/q)\exp(-E_a/RT)$.

We change the boundary value problem (Eqs. (11), (12)) into an initial value problem by solving the inert heat transport equation (derived by neglecting Ω in Eq. (11)),

$$\frac{\partial F_t}{\partial T} = \rho U C_p, \tag{A.2}$$

for T close to T_o to obtain the temperature gradient in the vicinity of T_o for an initial guess of S_l. Eq. (A.2) is integrated from T_o to T^* using a second-order Runge-Kutta method with variable step ΔT that exponentially increases with T. The distance x is integrated simultaneously using Eq. (12). The choice of T^* has little effect on the final solution as long as $q\rho\Omega(T^*)$ is small compared to $UC_p\mathrm{d}T/\mathrm{d}x$.

The computed x and $\mathrm{d}T/\mathrm{d}x$ at T^* are used as initial conditions to Eqs. (11) and (12), which are integrated using a second-order Runge-Kutta method with constant step Δx. The temperature gradient at $T = T_b = T_o + q/C_p$ depends on S_l, and the integration procedure is repeated with different S_l until the condition $\mathrm{d}T/\mathrm{d}x = 0$ when $T = T_b$.

Appendix B. 1D Steady-state detonation

For a 1D planar shock wave moving at D_{CJ} (Eq. (16)),

$$\frac{P_{ZND}}{P_o} = 2M_{CJ}^2\frac{\gamma}{\gamma+1} - \frac{\gamma-1}{\gamma+1}, \tag{B.1}$$

$$\frac{\rho_{ZND}}{\rho_o} = \frac{M_{CJ}^2(\gamma+1)}{M_{CJ}^2(\gamma-1)+2}, \tag{B.2}$$

$$e_{ZND} - e_o = 0.5(P_{ZND} + P_o)(1/\rho_o - 1/\rho_{ZND}), \tag{B.3}$$

where $M_{CJ} = D_{CJ}/c_o$ and $e_o = P_o/(\rho_o(\gamma-1))$. These ZND parameters ($P_{ZND}$, ρ_{ZND}, and e_{ZND}) are used as initial conditions for the integration of Eqs. (13)–(15). The equations are integrated using a second-order Runge-Kutta method from the initial conditions to the position x^* where $U = D_{CJ}\rho_o/\rho = c$. The half-reaction thickness, x_d is then defined as the distance between the leading shock wave and the point where half of the fuel has been consumed in the flame zone, i.e., where $Y = 0.5$.

References

[1] E.S. Oran, J.P. Boris, T. Young, M. Flanigan, T. Burks, T. Picone, Proc. Combust. Inst. 18 (1981) 1641–1649.
[2] J.W. Dold, A.K. Kapila, Combust. Flame 85 (1991) 185–194.
[3] J.Y. Chen, Combust. Sci. Technol. 57 (1988) 89–94.
[4] U. Maas, S.B. Pope, Combust. Flame 88 (1992) 239–264.
[5] A. Massias, D. Diamantis, E. Mastorakos, D.A. Goussis, Combust. Flame 117 (1999) 685–708.
[6] C.J. Montgomery, M.A. Cremer, J.Y. Chen, C.K. Westbrook, L.Q. Maurice, J. Propul. Power 18 (2002) 192–198.
[7] C.K. Westbrook, F.L. Dryer, Combust. Sci. Technol. 27 (1981) 31–43.
[8] D.J. Hautman, F.L. Dryer, K.P. Schug, I. Glassman, Combust. Sci. Technol. 25 (1981) 219–235.
[9] W.P. Jones, R.P. Lindstedt, Combust. Flame 73 (1988) 233–249.
[10] F.A. Williams, Private communication.
[11] A.M. Khokhlov, E.S. Oran, Combust. Flame 119 (1999) 400–416.
[12] E.S. Oran, A.M. Khokhlov, Philos. Trans. Roy. Soc. Lond. A 357 (1999) 3539–3551.
[13] A.M. Khokhlov, E.S. Oran, G.O. Thomas, Combust. Flame 117 (1999) 323–339.
[14] V.N. Gamezo, A.M. Khokhlov, E.S. Oran, Combust. Flame 126 (2001) 1810–1826.
[15] E.S. Oran, V.N. Gamezo, Combust. Flame 148 (2007) 4–47.
[16] V.N. Gamezo, T. Ogawa, E.S. Oran, Combust. Flame 155 (2008) 302–315.
[17] V.N. Gamezo, T. Ogawa, E.S. Oran, Proc. Combust. Inst. 31 (2007) 2463–2471.
[18] A.Y. Poludnenko, E.S. Oran, Combust. Flame 157 (2010) 995–1011.
[19] M. Kuznetsov, G. Ciccarelli, S. Dorofeev, V. Alekseev, Yu Yankin, T.H. Kim, Shock Waves 12 (2002) 215–220.
[20] C.T. Johansen, G. Ciccarelli, Combust. Flame 156 (2009) 405–416.
[21] V.N. Gamezo, T. Ogawa, E.S. Oran, Deflagration-to-detonation transition in H_2–air mixtures: effect of blockage ratio, in: 47th AIAA Aerospace Sciences Meeting and Exhibit, Orlando, Florida, AIAA 2009-440, 2009.
[22] V.N. Gamezo, A.M. Khokhlov, E.S. Oran, Secondary detonation cells in systems with high activation energy, in: 17th International Colloquium on Detonations, Explosions, and Reactive Systems, paper 237, 1999.
[23] V.N. Gamezo, A.A. Vasil'ev, A.M. Khokhlov, E.S. Oran, Proc. Combust. Inst. 28 (2000) 611–617.
[24] A.M. Khokhlov, Numerical study of the detonation wave structure in ethylene–oxygen mixtures, in: 42nd AIAA Aerospace Sciences Meeting and Exhibit, Reno, Nevada, AIAA Paper 2004-0792, 2004.
[25] Ya.B. Zeldovich, V.B. Librovich, G.M. Makhviladze, G.I. Sivashinsky, Astronaut. Acta 15 (1970) 313–321.
[26] G.E. Andrews, D. Bradley, Combust. Flame 19 (1972) 275–288.
[27] G.E. Andrews, D. Bradley, Combust. Flame 20 (1973) 77–89.
[28] G. Tsatsaronis, Combust. Flame 33 (1978) 217–239.
[29] A.I. Gavrikov, A.A. Efimenko, S.B. Dorofeev, Combust. Flame 120 (2000) 19–33.
[30] O. Peraldi, R. Knystautas, J.H. Lee, Proc. Combust. Inst. 22 (1986) 1629–1637.
[31] A. Veser, W. Breitung, S.B. Dorofeev, J. Phys. IV 12 (2002) 333–340.
[32] W. Breitung, S. Dorofeev, A. Kotchourko, R. Redlinger, W. Scholtyssek, Nucl. Eng. Des. 235 (2005) 253–270.
[33] R. Knystautas, J.H.S. Lee, J.E. Shepherd, A. Teodorczyk, Combust. Flame 115 (1998) 424–436.
[34] A. Teodorczyk, J.H.S. Lee, R. Knystautas, Proc. Combust. Inst. 22 (1988) 1723–1731.
[35] A. Teodorczyk, J.H.S. Lee, R. Knystautas, Prog. Astronaut. Aeronaut. 133 (1990) 233–240.
[36] A. Teodorczyk, Biul. Inst. Tech. Ciepl. Politech. Warsz. 79 (1995) 145–178.
[37] M.S. Kuznetsov, V.I. Alekseev, S.B. Dorofeev, Shock Waves 10 (2000) 217–223.
[38] S.B. Dorofeev, M.S. Kuznetsov, V.I. Alekseev, A.A. Efimenko, W. Breitung, J. Loss Prev. Process Ind. 14 (2001) 583–589.
[39] V.I. Alekseev, M.S. Kuznetsov, Y.G. Yankin, S.B. Dorofeev, J. Loss Prev. Process Ind. 14 (2001) 591–596.
[40] S.B. Dorofeev, J. Phys. IV 12 (2002) 3–10.
[41] M.S. Kuznetsov, V.I. Alekseev, Y.G. Yankin, S.B. Dorofeev, Combust. Sci. Technol. 174 (2002) 157–172.
[42] L.E. Fried, W.M. Howard, P.C. Souers, "CHEETAH 2.0 User's Manual," UCRL-MA-117541 Rev. 5, Lawrence Livermore National Laboratory, 1998.
[43] D.A. Kessler, V.N. Gamezo, E.S. Oran, Proc. Combust. Inst., submitted for publication.
[44] A.M. Khokhlov, J. Comput. Phys. 143 (1998) 519–543.
[45] D. Bradley, P.H. Gaskell, X.J. Gu, A. Sedaghat, Combust. Flame 143 (2005) 227–245.
[46] D. Bradley, M. Lawes, K. Liu, Combust. Flame 154 (2008) 96–108.
[47] J.H. Lee, R. Knystautas, C.K. Chan, Proc. Combust. Inst. 20 (1984) 1663–1672.
[48] S.B. Dorofeev, V.P. Sidorov, M.S. Kuznetsov, I.D. Matsukov, V.I. Alekseev, Shock Waves 10 (2000) 137–149.
[49] A.E. Lutz, R.J. Kee, J.A. Miller, H.A. Dwyer, A.K. Oppenheim, Proc. Combust. Inst. 22 (1988) 1683–1693.
[50] X.J. Gu, D.R. Emerson, D. Bradley, Combust. Flame 133 (2003) 63–74.